CONDENSED MATTER PHYSICS

Evolution and competition between chiral spin textures in nanostripes with D_{2d} symmetry

Jagannath Jena[1]*, Börge Göbel[1,2]*, Vivek Kumar[3], Ingrid Mertig[2], Claudia Felser[3], Stuart Parkin[1]†

Chiral spin textures are of considerable interest for applications in spintronics. It has recently been shown that magnetic materials with D_{2d} symmetry can sustain several distinct spin textures. Here, we show, using Lorentz transmission electron microscopy, that single and double chains of antiskyrmions can be generated at room temperature in nanostripes less than 0.5 μm in width formed from the D_{2d} Heusler compound $Mn_{1.4}Pt_{0.9}Pd_{0.1}Sn$. Typically, truncated helical spin textures are formed in low magnetic fields, whose edges are terminated by half antiskyrmions. These evolve into chains of antiskyrmions with increasing magnetic field. Single chains of these objects are located in the middle of the nanostripes even when the stripes are much wider than the antiskyrmions. Moreover, the chains can even include elliptical Bloch skyrmions depending on details of the applied magnetic field history. These findings make D_{2d} materials special and highly interesting for applications such as magnetic racetrack memory storage devices.

INTRODUCTION

Over the past decade, the observation of several noncollinear magnetic nano-objects has triggered enormous interest. Of special relevance for spintronic applications is the possibility of using these nano-objects as magnetic bits in racetrack data storage devices, namely, arrays of quasi one-dimensional nanostripes in which magnetic nano-objects are written, moved, read, and deleted (1). Despite recent progress using magnetic domain walls as the carriers of information (2, 3), the utilization of topologically protected nano-objects like magnetic skyrmions (4) or antiskyrmions (5, 6) is highly anticipated (7–11). These small magnetic whirls have high stability because of their topological nature, and they can be driven by comparably small currents (12, 13).

Because of their topological charge, skyrmions experience a deflection along a transverse direction (14–16) toward the edge of the racetrack, where they may become pinned or annihilate. Because of the rotational symmetry of skyrmions, this so-called skyrmion Hall effect is isotropic: It is present irrespective of the current orientation (17, 18). The reason is the stabilizing Dzyaloshinskii-Moriya interaction (DMI) (19–21) that arises from a broken inversion symmetry. At interfaces such as Fe/Ir (22), or in B20 materials like MnSi (4), the DMI leads to an isotropic canting of neighboring spins along all directions. This is not the case in materials that have, for example, a D_{2d} symmetry (magnetic point group $\overline{4}2m$) for which the inversion symmetry is broken so that the DMI vectors are anisotropic. For this reason, the ground-state spin textures in these materials are helices that are oriented along exactly two high-symmetry directions, and at elevated magnetic fields, antiskyrmions that are only rotational invariant after a 180° rotation form (21, 23). This implies that antiskyrmions behave differently under applied currents along different crystal directions, as simulated in (24). The aforementioned skyrmion Hall effect can even be absent for this special nano-object if the current is applied along a specific direction for which there is a particular magnetization profile of the antiskyrmion. Consequently, it is highly desirable to fabricate nanotracks along different crystallographic directions and to investigate the formation of differently oriented antiskyrmions.

A second advantage of systems with an anisotropic DMI is that the dipole-dipole interaction allows a coexistence of elliptically elongated skyrmions along with the DMI-mediated antiskyrmions, as was recently shown in lamellae formed from bulk samples of $Mn_{1.4}Pt_{0.9}Pd_{0.1}Sn$ (25, 26). If both nano-objects are metastable in a nanostripe, then "0" and "1" bits could be encoded by a sequence of skyrmions and antiskyrmions instead of the presence or absence of a single object at predefined positions. Using two distinct magnetic objects in a racetrack should make it less susceptible to diffusion or interactions between the topological objects that may be considerable in conventional racetracks (27–29).

Here, we prepare nanostripes of $Mn_{1.4}Pt_{0.9}Pd_{0.1}Sn$ along different crystallographic directions from bulk polycrystalline crystals. Using Lorentz transmission electron microscopy (LTEM), we investigate the magnetic texture and analyze the room temperature formation and stability of single and double chains of antiskyrmions in multiple geometries as well as helical spin textures from (to) which they can evolve with increasing (decreasing) magnetic field. The formation of these chains strongly depends on the field history and the initial magnetic configuration. We present several reliable ways to generate chains of antiskyrmions and observe an increased ease of the formation of antiskyrmions by comparison with extended films due to the confinement. This allows the generation of antiskyrmions without the need for the application of in-plane magnetic fields that was needed in extended lamellae (5, 6, 25). In these earlier studies on lamellae, the sample was tilted in the TEM to create an in-plane field and then tilted back for imaging. This "temporal" in-plane magnetic field helped to stabilize the antiskyrmions.

We show that a single chain of antiskyrmions can be formed in the middle of the track at room temperature, while recent observations in skyrmion systems revealed an edge-mediated nucleation of skyrmions at low temperatures (30–32) and densely filled skyrmion crystals at room temperature that are inconvenient for racetrack applications. Furthermore, we also observe the coexistence of antiskyrmions and two types of elliptically elongated skyrmions under

[1]Max Planck Institute of Microstructure Physics, Weinberg 2, 06120 Halle, Germany. [2]Institute of Physics, Martin Luther University Halle-Wittenberg, 06099 Halle, Germany. [3]Max Planck Institute for Chemical Physics of Solids, Nöthnitzer Strasse 40, 01187 Dresden, Germany.
*These authors contributed equally to this work.
†Corresponding author. Email: stuart.parkin@mpi-halle.mpg.de

certain conditions, which is promising for improving the reliability of magnetic racetrack devices.

RESULTS AND DISCUSSION

The investigated nanostripes were prepared from a single-crystalline grain of the polycrystalline bulk sample $Mn_{1.4}Pt_{0.9}Pd_{0.1}Sn$. A dual beam system ($Ga^+$ ion source) containing a focused ion beam (FIB) and a scanning electron microscope (SEM) was used during the lift-out process of the lamellae. The system is equipped with a gas injection system for the deposition of PtC_x as a protection layer during various steps of the fabrication process of the thin lamellae. PtC_x is also used as an adhesive for contacting the detached lamellae to an OmniProbe manipulator for subsequent attachment to a copper grid to allow ready transfer to the TEM. The embedded PtC_x on both sides of a nanostripe helps to reduce Fresnel fringing effects substantially. This allows a better LTEM contrast (30, 31, 33).

Because antiskyrmions are stabilized in the basal plane of the tetragonal inverse Heusler structure (5, 34), thin nanostripes oriented with the [001] direction perpendicular to the surface of the stripe are needed. This is confirmed by selected-area electron diffraction (SAED) before the magnetic textures are examined using the LTEM real-space imaging technique in which the electron beam is coincident at zero tilt angle with the sample's [001] crystal axis. The imaging is performed by a Lorentz mini lens, and the magnetic field is applied using the objective lens of the TEM: This field is directed along the column of the microscope. To realize in-plane components of magnetic field, the samples can be tilted a few degrees away from the TEM column axis by using a double-tilt sample holder.

Nanostripes along different crystallographic directions

Our main motivation is to investigate antiskyrmions in nanostripes whose long axis is oriented along different crystal directions. Figure 1A exemplarily shows how two stripes have been lifted out of the bulk sample. SEM overviews of two differently oriented stripes are shown in Fig. 1 (B and C). Figure 1 (D and E) shows TEM overviews of the same stripes. The ground-state helices in $Mn_{1.4}Pt_{0.9}Pd_{0.1}Sn$ are always oriented along the family of {10} directions because of the anisotropic DMI. For this reason, the orientation of the helix axes with respect to the nanostripe depends on the stripe orientation. In a [100] or [010] oriented nanostripe, the orientation of the helix axis with respect to the stripe direction, φ, can be 0° or 90°, whereas in a [110] or [1̄10] oriented nanostripe, φ = ±45°, as shown in Fig. 1 (F and G).

As mentioned above, antiskyrmions lack a continuous rotational symmetry due to the anisotropic DMI. The orientation of an antiskyrmion is strictly tied to the crystallographic axes of the host (5, 25). The profile of the magnetic texture of an antiskyrmion along the [100] or [010] directions corresponds to a Bloch wall, as indicated by the orange lines in Fig. 1H, whereas along the [110] or [1̄10] orientations, the magnetic texture profile corresponds to a Néel wall. In the LTEM images, only the Bloch parts give rise to any contrast. These are the bright and dark spots along the family of {10} directions with respect to the antiskyrmions' centers in Fig. 1 (I and J), which means that they are rotated when comparing both nanostripes. In the following, we will analyze antiskyrmions in confined nanostripes in more detail. For a confirmation of our interpretations of the LTEM results, we will refer to the results of micromagnetic simulations (see Materials and Methods for details), similar to Fig. 1 (K and L), where chains of antiskyrmions have been stabilized in both

nanostripes whose Bloch parts are always along the family of {10} directions.

Formation of helices and antiskyrmions in [010] oriented nanostripes

We begin our detailed analysis of the magnetic texture with a nanostripe that was cut along the [010] direction. Starting from the ferromagnetic state shown in Fig. 2A, decreasing the perpendicularly applied magnetic field leads to the generation of a helical phase with a wave vector (Q-vector) oriented perpendicularly to the nanostripe direction. While in zero magnetic field the spin texture of a helix in a D_{2d} material changes harmonically along the Q-vector, at increased fields the helix is distorted so that there are collinear ferromagnetic regions between individual segments of the helix (25). In the present nanostripes, the helix segments cannot be displaced from each other because of the confinement, which is why a different creation and annihilation mechanism has to be present. Starting from the ferromagnetic phase, at 227 mT, in Fig. 2B, a first helix segment forms that elongates upon further decreasing the field until it permeates the whole visible area of the nanostripe (Fig. 2C). Across this segment, the magnetization changes by 360° (it is parallel to the field direction at the edges and oppositely in the center). At lower fields, this process is repeated: first, with a second helix segment, as shown in Fig. 2 (D and E), and, later, with a third helix segment, as shown in Fig. 2 (F and G). The ratio of the area filled with helix segments over the ferromagnetic area is directly related to the external magnetic field, just as in extended films (25). However, because of the confinement, individual helix segments are generated or annihilated upon changing the field. This process is continuous, in the sense that an individual helix segment shrinks (elongates) upon increasing (decreasing) the magnetic field.

As observed, a helical phase with Q-vector along [100] is the ground state in the given nanostripe, while in an extended sample, helices with a Q-vector along the [010] direction are energetically equivalent. In a confined geometry, this latter state is less preferable energetically. A small number of long helix segments yield a lower energy than a larger number of short helix segments, because the edges of the segments cost energy, as they are highly noncollinear. However, when the field is decreased while tilting the sample, i.e., an in-plane field component is provided, this behavior changes, as is shown in Fig. 2 (H to N). Similar to extended lamellae, providing an in-plane magnetic field favors the generation of antiskyrmions over helices, because the energy barrier between these phases is decreased. In a field of 245 mT along the TEM column, when the sample is tilted by 21° in Fig. 2J, a periodic chain of nano-objects (5) has formed. Upon decreasing the field, at the same tilt angle, first, the number of these nanostructures increases further, partially leading to a zig-zag pattern due to the limited space in the nanostripe. However, at least in this measurement sequence, a dense zig-zag chain did not form. Instead, at further decreased fields, these distorted antiskyrmions start to elongate. Because of their interaction and the limited space along the nanostripe, the elongation is, this time, along the perpendicular direction [100] (see Fig. 2L). Slightly below zero field, all distorted antiskyrmions have turned into short helix segments and a periodic state has formed in Fig. 2N. This shows that, also in nanostripes, the magnetic texture is strongly dependent on the field history, similar to extended thin films (5, 25). Furthermore, if the field is decreased in an uncontrolled manner, e.g., by turning it off instantly, the resulting zero-field configuration consists
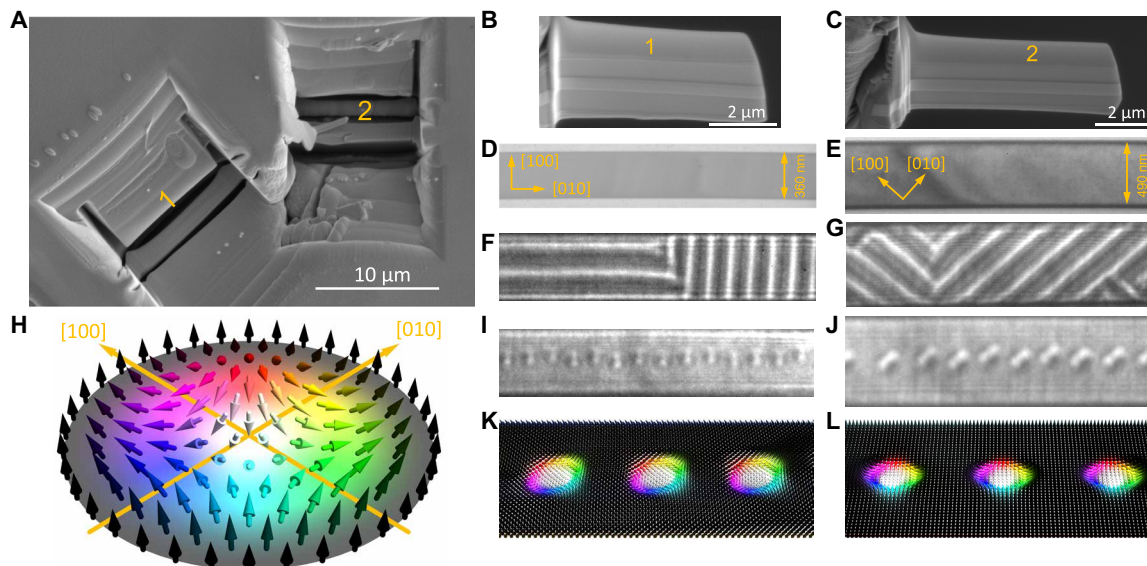
Fig. 1. Spin textures in oriented nanostripes. (**A**) SEM image of the host material after the nanostripes have been formed and lifted out by FIB. [010] and [$\bar{1}$10] oriented nanostripes that were fabricated from (A) are shown in the SEM images in (**B**) and (**C**). (**D** and **E**) Bright-field TEM images of portions of nanostripes with indicated widths and crystallographic axes. (**F** and **G**) Lorentz TEM images of the magnetic texture at zero field in the two nanostripes that show the formation of helices whose Q-vectors are oriented along the [100] and [010] directions, in both cases. (**H**) Schematic representation of a magnetic antiskyrmion, where the color encodes the orientation of the magnetic moments. The Bloch parts of the antiskyrmion are along the family of {10} directions (orange), while the Néel parts are along the {11} directions. (**I** and **J**) LTEM images of antiskyrmion chains measured in magnetic fields of 187 and 273 mT, respectively, oriented perpendicular to the plane of the nanostripes. The bright and dark regions correspond to the antiskyrmions' Bloch parts oriented along {10}. (**K** and **L**) Micromagnetic simulations of the spin textures in nanostripes with orientations corresponding to those in (I) and (J), respectively. The color code represents the direction of the moment within each cell used in the simulation. The same color code has been used throughout the paper: black along +z, white along −z, and the hue colors stand for in-plane orientations with respect to the [100] direction (e.g., blue arrows always point along the [100] direction).
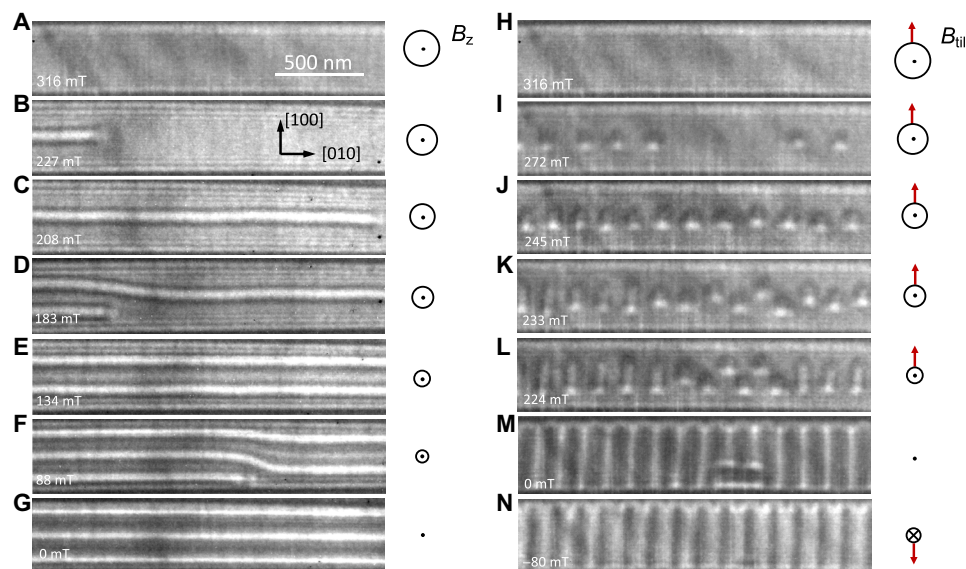

Fig. 2. Helix formation upon decreasing the magnetic field. In the left column, the magnetic field is decreased starting from 316 mT in (**A**) corresponding to the ferromagnetic phase. (**B**) At 227 mT, a single helix segment forms along the [010] direction (along the nanotrack), elongates, and finally extends over the whole stripe region in (**C**) at 208 mT. (**D**) At 183 mT, a second helix segment forms, which elongates in (**E**) at 134 mT. (**F**) At 88 mT, a third segment forms. (**G**) At zero field, the ground state is formed: three parallel helix segments along the nanostripe. In the right row, the magnetic field is decreased under tilting of the sample by ~21°. (**H**) The starting configuration is again the ferromagnetic phase at 316 mT. (**I**) At 272 mT, noncollinear spin textures already form at higher magnetic fields. An irregular chain of antiskyrmions has formed. (**J**) At 245 mT, more of those have formed and the chain is rather periodic. (**K**) At 233 mT, they begin to elongate along the [100] direction (perpendicular to the nanotrack direction). (**L**) At 224 mT, a mixed state has formed. (**M**) At zero field, the magnetic texture is not perfectly ordered. (**N**) At small negative fields, a periodic helical state is formed. Using this tilted field, the helical segments are oriented along the [100] direction rather than [010].

of several helix domains either oriented along the [100] or [010] directions.

In Fig. 3, we show the behavior of the magnetic texture upon increasing the magnetic field from the three aforementioned starting configurations. In Fig. 3A, the helix Q-vector is along the [100] direction, i.e., the helix segments are elongated along the nanostripe. The increasing field behavior is roughly the reversal of the decreasing field behavior (Fig. 3, B to E). The helix segments shrink and disappear one after another. Likewise, when the starting configuration consists of a helix with a Q-vector along [010] (Fig. 3F), the increasing field behavior is similar to the decreasing field behavior. The helix segments that are perpendicular to the nanostripe shrink (Fig. 3G) until a periodic chain of antiskyrmions is formed (Fig. 3H). Upon further increasing the field, the nano-objects disappear, one after another (Fig. 3I), until the ferromagnetic state is restored. Note that in this particular image it is difficult to tell the exact texture of these individual objects because of their decreased size. Besides antiskyrmions, they could be elliptical skyrmions or even trivial bubbles, as observed in extended samples (25).

What is, however, notable is that this time the field is increased without providing an in-plane field component and antiskyrmions form anyway. This implies that the truncated helix segments at zero field are still topologically nontrivial. The results of micromagnetic simulations (Fig. 3, P to R) reveal that each helix segment consists of a topologically trivial center part that can have different lengths. However, the helix edges always exhibit the profile of half an antiskyrmion, each due to the anisotropic DMI that leads to the same edge twist even for differently shaped objects: For example, the upper edges of the helix segments in Fig. 3R and the antiskyrmions in Fig. 3Q have the same in-plane configuration (red-orange-yellow-green color code), independent of the shape of the object. Therefore,

both edge parts of a helix segment have a topological charge of $^1/_2$ each. An individual helix segment can be considered an "elongated antiskyrmion."

Antiskyrmion formation without providing in-plane fields was not observed in extended thin films so far, pointing toward an increased stability of antiskyrmions in confined geometries and a new nucleation mechanism. The shrinking helix mechanism for antiskyrmion generation is directly related to the confinement. Following the one-to-one correspondence of helix segments and antiskyrmions in the case of vertically oriented helix segments (Fig. 3, F to J), it is conceivable that horizontally oriented helix segments also condense to single antiskyrmions. However, because in a perfect sample only three helix segments permeate the whole nanostripe, the resulting antiskyrmion density is vanishingly small in this procedure and no antiskyrmions are visible in Fig. 3 (A to E).

Furthermore, it is worth mentioning that, although the formation of the antiskyrmions is strongly affected by the confinement, the antiskyrmions always form in the middle of the nanostripe, unlike edge-mediated skyrmions presented in the B20 material FeGe (30, 33). We repeated these experiments for a wider nanostripe with a width of 490 nm (see Fig. 1J) and find again that the antiskyrmions always form in the middle of the nanostripe.

Repeating the increasing field experiment starting from the mixed helical configuration (Fig. 3K) is particularly interesting, as it reveals more about the interaction of helix segments and antiskyrmions. The starting configuration consists of one horizontal helix segment at the bottom in Fig. 3K. The rest of the racetrack is filled with vertical segments on the right side and two more horizontal segments on the left side. Upon increasing the magnetic field to 158 mT in Fig. 3L, the vertical helix segments begin to shrink and one of the upper horizontal segments disappears. When the field is further increased
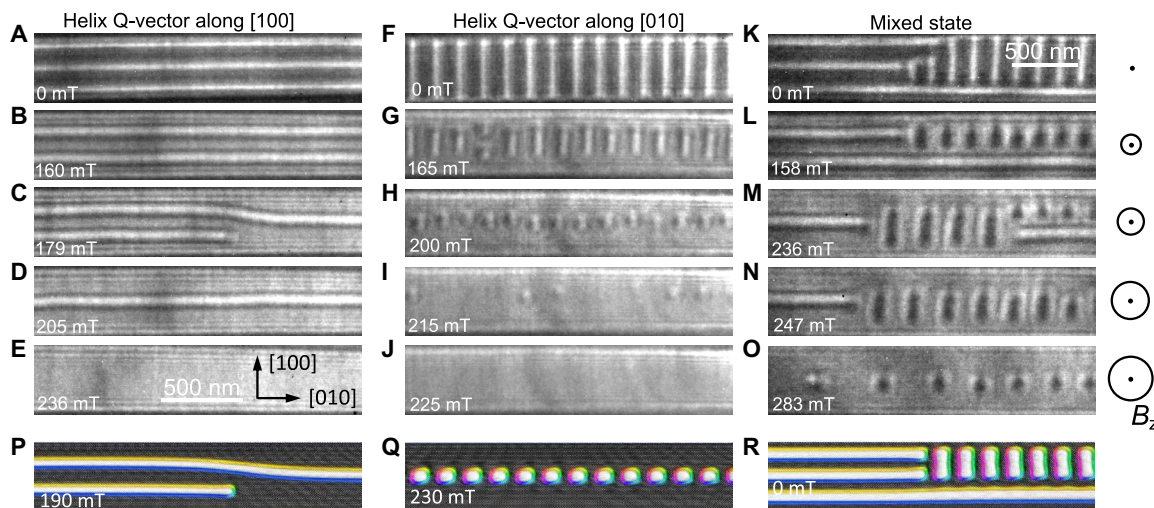

Fig. 3. Antiskyrmion and helix formation upon increasing the magnetic field. On the left side, the starting configuration (**A**) is a helical phase with helix segments along [010]. (**B** to **E**) The three individual segments shrink and disappear one after another upon increasing the magnetic field as indicated. In the middle column, the helix segments are initially oriented along the [100] direction, the narrow width of the nanostripe (**F**). (**G**) Again, they shrink, but this time, antiskyrmions form in (**H**) at 200 mT. (**I**) At 215 mT, the antiskyrmions annihilate. (**J**) At 225 mT, the ferromagnetic phase is restored. In the right column, the initial configuration (**K**) is a mixed helical state with Q-vectors along [100] and [010]. (**L**) At 158 mT, the helix segments shrink. (**M**) At 236 mT, the interaction of them leads to segments of different sizes along [100]. (**N**) Once the helix segment at the bottom right edge has disappeared, the smaller segments expand upon relaxation. (**O**) Even at 283 mT, the antiskyrmion on the very left has a slightly different contrast compared to the other antiskyrmions. This is because small deformations along [100] and [010] are still present, corresponding to the initial helix type. (**P** to **R**) Results of micromagnetic simulations exemplarily showing the metastability of (P) a mixture of one and two horizontal helix segments, (Q) a chain of antiskyrmions, and (R) a mixture of horizontal and vertical helix segments (see Materials and Methods for details).

in Fig. 3M, the long horizontal helix segment shrinks and is only visible on the right side of the stripe region shown. Consequently, the vertically oriented segments in the middle can elongate again, and the one remaining horizontal segment on the left moves to the middle of the racetrack. Near the transition to the ferromagnetic phase in Fig. 3O, all helix segments have shrunk and formed antiskyrmions. Reminiscent of the initial helix orientation, a small deformation is still present for the antiskyrmions in this LTEM image. The antiskyrmion on the left has a notably different contrast, indicating elongation along the racetrack, while the others are slightly elongated along the perpendicular direction.

Our measurements of the LTEM contrast can qualitatively be accounted for by micromagnetic simulations: Figure 3P shows the stability of an extended helix and another helix that starts in the middle of the frame. The longer helix segment is located in the middle of the stripe in the right part of the track but is shifted to the top in the left half where the second helix segment is present, similar to the experimental observations. Furthermore, upon slightly increasing the field, the shorter helix segment shrinks, while it increases its size upon decreasing the field. In Fig. 3Q, a chain of antiskyrmions is present, qualitatively reproducing the experimental findings from Fig. 3H. Figure 3R shows the metastability of a mixed helical phase. These simulations were each initialized with a different analytically constructed magnetization density that was relaxed (see Materials and Methods for details).

Antiskyrmion chains in differently oriented nanostripes

We now investigate a lamella where the nanostripe orientation is rotated by $\varphi \approx -28°$ (i.e., in clockwise direction) with respect to the [100] crystallographic axis. In Figs. 4 and 5, the decreasing and increasing field behaviors of the magnetic texture are shown in this nanostripe.

Again, the ground state is the helical phase. This time, the helix Q-vectors are rotated by φ compared to the helices in the nanostripe discussed above. This can be contrasted with B20 materials, where the confined geometry of a nanostripe induces a strong anisotropy to the helix orientation so that they always form perpendicular or parallel to the edge, as discussed in (30, 33). Although the two types of helices are not aligned parallel or perpendicular to the nanostripe direction in the D_{2d} system for the nanostripe shown in Figs. 4 and 5, one of the two helix types exhibits longer segments than the other when these permeate the whole width of the nanostripe. Similar to the case presented above, the helical phase with the longer segments has the lower energy; since then, the density of the ends of the helices is decreased. Because of this special feature of textures in such a confined geometry, the starting configuration (shown in Fig. 4A) consists of helix segments that are oriented along a direction rotated by φ with respect to the nanostripe direction [100]. Upon increasing the field (Fig. 4, B to E), the lengths of the segments shrink until antiskyrmions are formed. In good qualitative agreement with the theoretical predictions, the two bright and dark spots in the LTEM contrast are rotated by $\varphi - 90°$ compared to the antiskyrmions in Fig. 3, pointing toward the anisotropic properties of antiskyrmions. At higher fields, the antiskyrmions annihilate. When the field is increased to 253 mT in Fig. 4F, only a single nano-object is left. At slightly higher fields, this object disappears.

The formation of an antiskyrmion chain without providing in-plane magnetic fields (which would be unfavorable for spintronic devices) is very interesting for racetrack applications. The mecha-

nism relies on the fact that the helix segments are truncated at the edges, and it is therefore highly relevant in our confined geometries compared to extended samples. We now compare this mechanism for antiskyrmion nucleation in nanostripes to the more conventional mechanism (that uses tilting) that we have extensively explored in extended thin lamellae (5, 25, 26). The effect of temporal in-plane fields was investigated by tilting the sample by ~30° after each increase in field and then back to zero tilt once the target field was reached. We find that, now, a double row of antiskyrmions can sometimes be formed rather than a single row. As explained, the topology of the truncated helices and the single row of antiskyrmions is the same, and so, they can easily transform from one to the other. On the other hand, there needs to be a topological transformation when the truncated helices transform into a double row of antiskyrmions, so in this case, an energy barrier has to be overcome. Tilting provides an in-plane field component that helps overcome this energy barrier. Thus, there are two distinct mechanisms for the transformation of the truncated helices into antiskyrmions. Figure 4 (A to L) compares a sequence of LTEM images for the same nanostripe with and without this tilting procedure as the field is increased from zero. A similar behavior is seen at low fields whether tilting is used or not: The helical phase is found. In the field range starting from ~190 mT, we observe a double row of antiskyrmions for the case of tilting, instead of a single row without tilting. When the field is increased without tilting (Fig. 4, A to F), the helix segments shrink to antiskyrmions and no "new" antiskyrmions are formed. With tilting (Fig. 4, G to L), the topologically induced energy barrier can be overcome and we find a greater density of antiskyrmions. Figure 4M quantitatively shows how the number of antiskyrmions increases because of tilting. This is similar to extended thin lamellae, where a temporal in-plane magnetic field leads to the formation of a hexagonal lattice of antiskyrmions (5, 25). Here, in the nanostripes, this lattice appears in its minimal shape: A zig-zag chain of antiskyrmions can be seen as a precursor of the antiskyrmion lattice. When the field is increased further, the antiskyrmions start to annihilate one after another both with and without tilting. For the case of tilting, the double row evolves into a single antiskyrmion chain at ~237 mT (Fig. 4K), and at even higher fields, the ferromagnetic phase is restored.

We have also investigated the dependence of the antiskyrmion formation on the tilting angle. For small tilt angles (<~25°), no double rows of antiskyrmions are found. The in-plane field component (that increases with tilt angle) is not large enough to overcome the energy barrier between the truncated helices and the double chain of antiskyrmions. Consequently, only a single row of antiskyrmions forms. For large tilting angles (see fig. S1 for LTEM contrasts for a tilting angle of 38°), we qualitatively see the same behavior as for 30° (described above). However, the double row of antiskyrmions forms at lower total magnetic fields. This stems from the fact that the in-plane field component, which is necessary for the formation of a double row of antiskyrmions, is already reached at a smaller total field. Furthermore, the antiskyrmions in the double row are more densely packed. On the other hand, the critical field that characterizes the transformation from a double to a single row of antiskyrmions at high fields is insensitive to tilting angle because this mechanism is not related to the tilting. It is rather a regular transition to the ferromagnetic phase. These results are summarized in Fig. 4M and underline our interpretation of two separate mechanisms for the antiskyrmion formation: one caused by the topological equivalence of
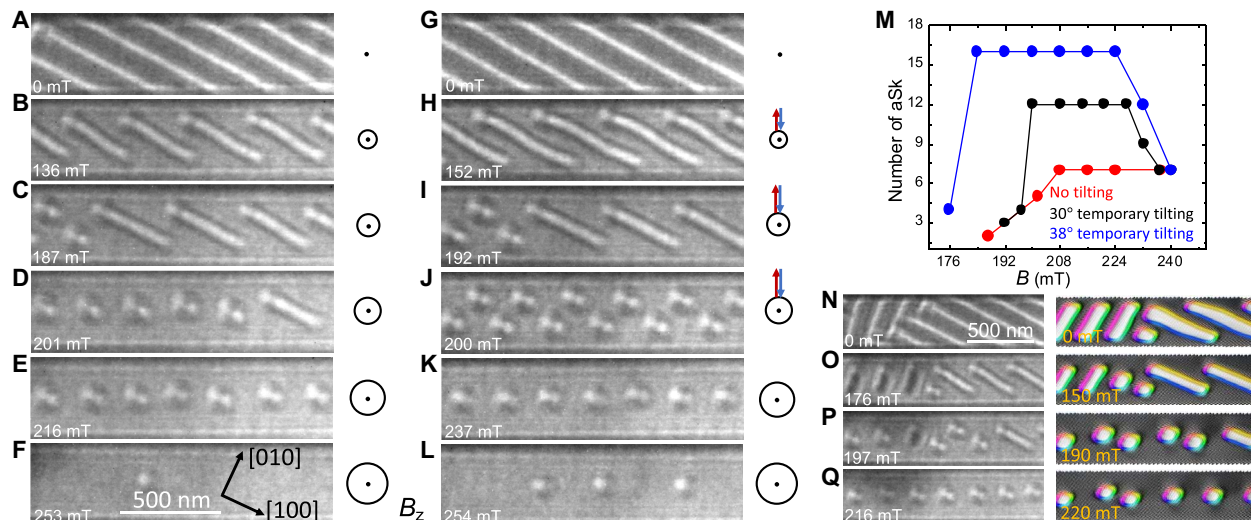
Fig. 4. Single and double chains of antiskyrmions. In the left column, the starting configuration (**A**) are helix segments that are elongated along the [100] direction, which is oriented at an angle $\varphi \approx -28°$ with respect to the racetrack direction. (**B**) Upon increasing the field, the helix segments shrink, until few antiskyrmions are formed in (**C**) at 187 mT. (**D**) For fields above 201 mT, almost all segments have turned into antiskyrmions so that a chain of antiskyrmions is present in (**E**). (**F**) At 253 mT, the antiskyrmions annihilate, until the ferromagnetic phase is restored. In the middle column, the procedure is changed. This time, the sample is reversibly tilted by 30° to provide a temporal in-plane field component before each image is taken. (**G** to **I**) At low fields, the magnetic texture mainly exhibits a helical phase, like in the left column. (**J**) However, at 200 mT, a double row of antiskyrmions forms because of temporary application of in-plane field component. (**K**) At 237 mT, the number of antiskyrmions reduces and a single chain is restored. At 254 mT, the sample becomes ferromagnetic in (**L**). In (**M**), the numbers of antiskyrmions (aSk) for the two scenarios are compared for different field strengths (red is without in-plane field; black is with in-plane field). Blue shows results for a larger tilting angle. The corresponding LTEM images are shown in the Supplementary Materials (fig. S1). In (**N** to **Q**), the generation of an antiskyrmion chain starting from a mixed helical phase is shown. Like in the left column, the magnetic field is not tilted in this this case. On the right side, results of micromagnetic simulations are shown. Both helix types from (N) shrink and form antiskyrmions in (Q).

single rows of antiskyrmions and truncated helix segments (only important in nanostripes) and the other caused by in-plane fields (important in nanostripes and in extended thin samples).

Concerning the helix orientation with respect to the nanostripe orientation, for the aforementioned geometrical reasons, the closer φ is to 45°, the closer the two helical orientations are in energy. In such a case, the formation of helical domains becomes inevitable. Therefore, the behavior of the magnetic texture was also investigated as the field is increased when the starting configuration is a multi-domain helical phase. Figure 4 (N to Q) shows a nanostripe with $\varphi \approx -28°$ as in the above, but in which two helices can be seen with Q-vectors approximately along the [100] and [010] axes. In Fig. 4N, it becomes apparent that the helix orientation is slightly affected by the edge interaction. The two types of helix segments do not form at an angle of exactly 90° (but ±4°), as distinct from helices in extended lamellae. Furthermore, the corresponding helix segments have different lengths. When the field is increased, both types of helices shrink until a single chain of antiskyrmions is formed in Fig. 4Q. A qualitatively similar behavior is found in the micromagnetic simulations when starting from a mixed helical phase.

When we decrease the field starting from the ferromagnetic phase (Fig. 5A), we also find a distinct behavior. When we do not provide a temporal in-plane field, antiskyrmions form at fields near 216 mT in Fig. 5B. This was not the case for the initially investigated nanostripe that was oriented along the high-symmetric [010] direction. Instead of forming one single helix segment that elongates along the track, in the present nanostripe many antiskyrmions form, because a single helix segment cannot elongate much due to the considerable angle φ between the nanotrack orientation and the high-symmetry

directions. Upon further decreasing the field, the antiskyrmions elongate along [100], which is the longer of the two possible helix directions (Fig. 5, C to G). When we instead provide a temporal in-plane magnetic field, we find a different behavior. First, we see only a few antiskyrmions in Fig. 5H at a field of 215 mT. At a decreased field of 211 mT, more antiskyrmions are present and constitute a dense chain in Fig. 5I. At a field of 192 mT, enough antiskyrmions are present that a zig-zag double chain forms in Fig. 5J. When we decrease the field again, we can see how the antiskyrmions in this double chain elongate (Fig. 5, K to M). Again, they do this along the [100] direction, but because of the limited space, they cannot elongate to permeate the whole width of the nanostripe. At zero field, the helical phase is restored (Fig. 5N).

In Fig. 5 (O and Q), the metastability of single and double anti-skyrmion chains is shown from the results of micromagnetic simulations. Upon decreasing the magnetic field, the antiskyrmions elongate along the [100] direction in both cases (Fig. 5, P and R), similar to the experiment.

Coexistence of skyrmions and antiskyrmions

Recently, in (*25*), we showed the coexistence of antiskyrmions and elliptically deformed skyrmions in $Mn_{1.4}Pt_{0.9}Pd_{0.1}Sn$ extended lamellae [also independently observed in (*26*)]. The elliptical skyrmions are of the Bloch type. They are stabilized by dipole-dipole interactions that allow both Bloch chiralities. Depending on the chirality, the anisotropic DMI then leads to their elongation along the [100] or [010] direction, respectively.

In our nanostripes, we also find elliptical skyrmions. Figure 6 shows LTEM images of the magnetic texture in a $\varphi \approx 45°$ nanostripe for various temporal tilting angles. The Bloch skyrmions appear as
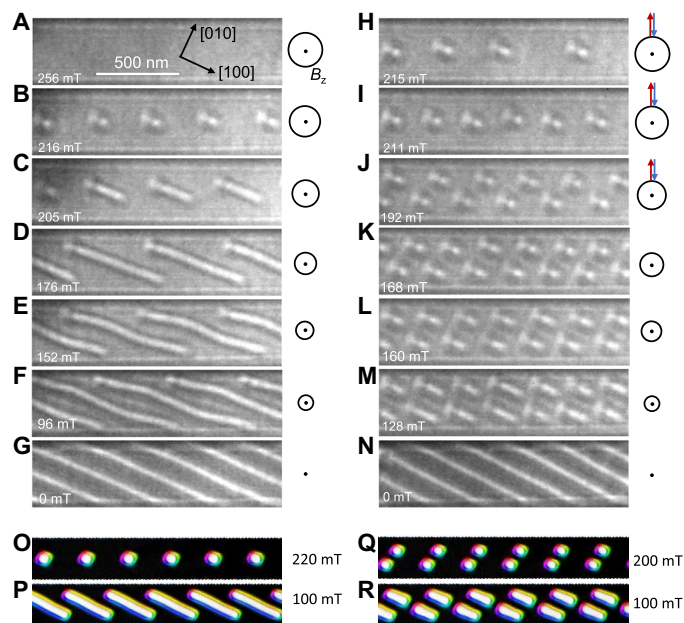
Fig. 5. Evolution of single and double antiskyrmion chains upon decreasing the field. In the left column, (**A**) the starting configuration is a ferromagnet. (**B**) The field is simply decreased, leading to the generation of antiskyrmions. (**C** to **G**) The antiskyrmions elongate until a helical phase is restored. In the right column, the starting configuration is again a ferromagnet. (**H**) This time, the field is reduced under reversible tilting of the sample by 30° to provide a temporal in-plane magnetic field. This again allows the stabilization of antiskyrmions. (**I**) They survive at 211 mT without elongation. (**J**) At 192 mT, a double chain of antiskyrmions forms. (**K** to **M**) When the field is decreased from here, these double chains of antiskyrmions elongate. (**N**) At zero field, the helical phase is restored. (**O** and **P**) The elongation process of an antiskyrmion chain is shown in micromagnetic simulations at different external fields. (**Q** and **R**) When more antiskyrmions are placed in the sample, a double chain of antiskyrmions is stabilized that elongates similar to the experiments.

elliptical objects with a dark center and a bright ring outside when elongated along the [010] direction or as elliptical objects with a bright center and a dark ring outside when elongated along the [100] direction. Our starting configuration is a chain of antiskyrmions that has been generated using tilting, as discussed above. Here, we already find a few elliptical skyrmions.

The reason is that small temporal in-plane fields stabilize the formation of elliptical skyrmions. In Fig. 6B, the temporal tilting angle used was only 1.3°. As a result, all the antiskyrmions have turned into Bloch elliptical skyrmions. Arguably, for some of them, it is not possible to unambiguously determine their exact magnetic state, but a comparison with the initial configuration (Fig. 6A) shows that the magnetic contrast has changed. When we now use a larger tilting temporal angle, we again find more antiskyrmions (i.e., 12 antiskyrmions versus 11 skyrmions in Fig. 6C). The experiment was operated with multiple temporal tilting angles until, at a tilting angle of 27°, the texture mainly consists of antiskyrmions (Fig. 6E), as was presented in the cases above. Repeating these experiments at tilting angles of 1.3° and 27° several times gave identical results: a single chain of skyrmions versus a single chain of mostly antiskyrmions.

In Fig. 6G, we show that elliptical skyrmions and antiskyrmions can be stabilized in micromagnetic simulations of a nanostripe, similar to our experiments, when the anisotropic DMI and the dipole-dipole interaction are considered. For the simulation parameters that are

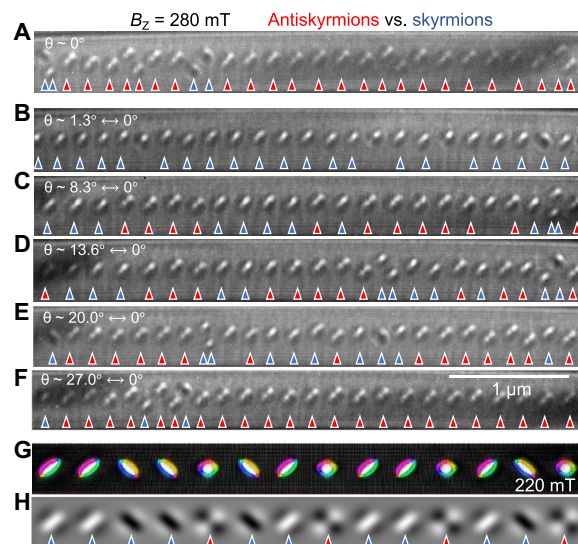
Fig. 6. Antiskyrmions versus elliptical skyrmions in a nanostripe along the [$\bar{1}$10] direction. In (**A**), the initial configuration is shown consisting mainly of antiskyrmions (indicated by red triangles) and only showing three elliptical skyrmions that are elongated along the [010] direction and one elliptical skyrmion that is elongated along the [100] direction (both indicated by blue triangles). In (**B**), the sample was reversibly tilted to provide a small in-plane field along the [100] direction. The result is mainly elliptical skyrmions. Most of them are elongated along the [100] direction. In (**C** to **F**), the same procedure is repeated but with larger tilting angles: The number of antiskyrmions increases with tilt angle. For a few nano-objects, it is difficult to determine whether it is a skyrmion or an antiskyrmion. In these cases, we did not add a marker. In (**G**), the coexistence of elliptical Bloch skyrmions and antiskyrmions in a single chain is shown as a result of a micromagnetic simulation. (**H**) Simulated LTEM contrast of the spin texture shown in (G).

used (see Materials and Methods), both objects are stable for fields up to 220 mT. Figure 6H shows the corresponding simulated LTEM contrast. It becomes apparent that antiskyrmions and one type of elliptical skyrmion look rather similar, explaining why it is sometimes difficult to distinguish antiskyrmions and elliptical skyrmions in the LTEM experiment. In a device, they could be distinguished electrically by their different Hall signatures.

In summary, we have demonstrated two major findings. First, that single chains of antiskyrmions are formed along the middle of nanostripes formed from a D_{2d} material even when the stripe is much wider than the individual antiskyrmions and without providing any in-plane magnetic field. This nucleation mechanism is related to the topological equivalence of antiskyrmions and truncated helix segments. It is relevant in confined geometries and is distinct from the temporal in-plane field mechanism described for extended thin lamellae in our previous studies. Second, these chains of antiskyrmions can coexist with elliptical Bloch skyrmions. Because these findings take place at room temperature, it makes them a highly attractive feature of D_{2d} systems and conceptually suggests the possibility of robust memory or computing devices that could encode data in such systems in two distinct topologically protected objects.

MATERIALS AND METHODS
Specimen preparation
Polycrystalline ingots of $Mn_{1.4}Pt_{0.9}Pd_{0.1}Sn$ were prepared by arc-melting methods. The detailed preparation as well as structural and

magnetic characterization are described in [5]. Nanostripe lamellae were prepared in a FEI NanoLab DualBeam system that has both a SEM and a FIB equipped with a gas injection system and a micromanipulator (Oxford OmniProbe 200+). The final polishing was done at 2 kV to remove any damaged surface material. Four different nanostripe lamellae are used in this study, all prepared with the same method. The thicknesses are ~100 nm for Figs. 1 (F and I), 2, and 3, ~200 nm for Fig. 1 (G and J), and nearly 150 nm for the stripe in Figs. 4 and 5 as well as for the stripe in Fig. 6.

Lorentz TEM measurements

The observation of magnetic contrast was carried out in a TEM (FEI, Titan 80-300kV) equipped with an electrostatic mini-lens for Lorentz imaging. The objective lens of the TEM was used to realize magnetic fields along the microscope axis corresponding to zero tilt of the sample. A double tilt sample holder was used. SAED was used to identify grains within the polycrystalline sample that were oriented with the [001] axis at zero tilt. All LTEM images were taken with defocus values between 1.1 and 1.2 nm.

Micromagnetic simulations

Micromagnetic simulations were carried out using mumax^3 [35, 36]. This program propagates the Landau-Lifshitz-Gilbert equation [37, 38] for every discretized magnetization cell according to

$$\dot{\mathbf{m}} = -\gamma_e \, \mathbf{m} \times \mathbf{B}_{\text{eff}} + \alpha \, \mathbf{m} \times \dot{\mathbf{m}}$$

Here, $\mathbf{m}$ is the normalized moment, γ_e is the gyromagnetic ratio of an electron, $\alpha = 0.3$ is the Gilbert damping parameter, and $\mathbf{B}_{\text{eff}} = -\frac{\delta F}{M_S \delta \mathbf{m}}$ is the effective magnetic field. This quantity is derived from the free energy density F for which the Heisenberg exchange, a uniaxial magnetic anisotropy, the external magnetic field, and dipole-dipole interactions have been included. Furthermore, we implemented an anisotropic DMI that corresponds to the D_{2d} symmetry of the crystals under study. We take parameters from [25]: the measured saturation magnetization $M_S = 445$ kA/m and the DMI constant $D = 0.003$ J/m^2. The exchange interaction $A_{\text{ex}} = 0.5 \times 10^{-10}$ J/m and the anisotropy constant $K_u = 135$ kJ/m^3 had to be reduced to fit the experimental results better. The magnetic field strength is indicated in the respective image. In all simulations, periodic boundary conditions are applied along the track. The simulated length is 4200 nm; the thickness is 150 nm, and the width is 400 or 600 nm. In most cases, only half of the simulated length is shown in the figure. The magnetization density was discretized in 10 nm × 10 nm × 10 nm cells, except for Fig. 6 where a finer grid of 2.5 nm × 2.5 nm × 10 nm was necessary. We also checked the stability of elliptical skyrmions and antiskyrmions in a finite geometry and stabilized all shown textures using the direct energy minimization solver ("minimize") based on the conjugate gradient method.

Lorentz TEM simulations

We simulated the LTEM image in Fig. 6H using the method presented in our earlier publication [25]. The transmitted electron density, i.e., the LTEM contrast, is given as

$$\int \exp\left\{-\left[(x - d \cdot m_y(x', y') - x')^2 + (y + d \cdot m_x(x', y') - y')^2\right]/a^2\right\} \, dx' \, dy'$$

The average magnetization of all layers leads to a deflection (maximum $d = 2$ nm) of the incoming electron beams according to the Lorentz force. The individual beams have been modeled by a Gaussian function with a smearing factor $a = 60$ nm.

SUPPLEMENTARY MATERIALS

REFERENCES AND NOTES

1. S. S. P. Parkin, M. Hayashi, L. Thomas, Magnetic domain-wall racetrack memory. *Science* **320**, 190–194 (2008).
2. S.-H. Yang, C. Garg, S. S. P. Parkin, Chiral exchange drag and chirality oscillations in synthetic antiferromagnets. *Nat. Phys.* **15**, 543–548 (2019).
3. R. Duine, K.-J. Lee, S. S. P. Parkin, M. D. Stiles, Synthetic antiferromagnetic spintronics. *Nat. Phys.* **14**, 217–219 (2018).
4. S. Mühlbauer, B. Binz, F. Jonietz, C. Pfleiderer, A. Rosch, A. Neubauer, R. Georgii, P. Böni, Skyrmion lattice in a chiral magnet. *Science* **323**, 915–919 (2009).
5. A. K. Nayak, V. Kumar, T. Ma, P. Werner, E. Pippel, R. Sahoo, F. Damay, U. K. Rößler, C. Felser, S. S. P. Parkin, Magnetic antiskyrmions above room temperature in tetragonal Heusler materials. *Nature* **548**, 561–566 (2017).
6. J. Jena, R. Stinshoff, R. Saha, A. K. Srivastava, T. Ma, H. Deniz, P. Werner, C. Felser, S. S. P. Parkin, Observation of magnetic antiskyrmions in the low magnetization ferrimagnet Mn$_2$Rh$_{0.95}$Ir$_{0.05}$Sn. *Nano Lett.* **20**, 59–65 (2019).
7. R. Tomasello, E. Martinez, R. Zivieri, L. Torres, M. Carpentieri, G. Finocchio, A strategy for the design of skyrmion racetrack memories. *Sci. Rep.* **4**, 6784 (2014).
8. A. Fert, V. Cros, J. Sampaio, Skyrmions on the track. *Nat. Nanotechnol.* **8**, 152–156 (2013).
9. J. Iwasaki, M. Mochizuki, N. Nagaosa, Current-induced skyrmion dynamics in constricted geometries. *Nat. Nanotechnol.* **8**, 742–747 (2013).
10. J. Sampaio, V. Cros, S. Rohart, A. Thiaville, A. Fert, Nucleation, stability and current-induced motion of isolated magnetic skyrmions in nanostructures. *Nat. Nanotechnol.* **8**, 839–844 (2013).
11. A. O. Leonov, M. Mostovoy, Edge states and skyrmion dynamics in nanostripes of frustrated magnets. *Nat. Commun.* **8**, 14394 (2017).
12. F. Jonietz, S. Mühlbauer, C. Pfleiderer, A. Neubauer, W. Münzer, A. Bauer, T. Adams, R. Georgii, P. Böni, R. A. Duine, K. Everschor, M. Garst, A. Rosch, Spin transfer torques in MnSi at ultralow current densities. *Science* **330**, 1648–1651 (2010).
13. X. Yu, N. Kanazawa, W. Zhang, T. Nagai, T. Hara, K. Kimoto, Y. Matsui, Y. Onose, Y. Tokura, Skyrmion flow near room temperature in an ultralow current density. *Nat. Commun.* **3**, 988 (2012).
14. W. Jiang, X. Zhang, G. Yu, W. Zhang, X. Wang, M. B. Jungfleisch, J. E. Pearson, X. Cheng, O. Heinonen, K. L. Wang, Y. Zhou, A. Hoffmann, S. G. E. te Velthuis, Direct observation of the skyrmion Hall effect. *Nat. Phys.* **13**, 162–169 (2017).
15. S. Woo, K. Litzius, B. Krüger, M.-Y. Im, L. Caretta, K. Richter, M. Mann, A. Krone, R. M. Reeve, M. Weigand, P. Agrawal, I. Lemesh, M.-A. Mawass, P. Fischer, M. Kläui, G. S. D. Beach, Observation of room-temperature magnetic skyrmions and their current-driven dynamics in ultrathin metallic ferromagnets. *Nat. Mater.* **15**, 501–506 (2016).
16. K. Litzius, I. Lemesh, B. Krüger, P. Bassirian, L. Caretta, K. Richter, F. Büttner, K. Sato, O. A. Tretiakov, J. Förster, R. M. Reeve, M. Weigand, I. Bykova, H. Stoll, G. Schütz, G. S. D. Beach, M. Kläui, Skyrmion Hall effect revealed by direct time-resolved x-ray microscopy. *Nat. Phys.* **13**, 170–175 (2017).
17. J. Iwasaki, M. Mochizuki, N. Nagaosa, Universal current-velocity relation of skyrmion motion in chiral magnets. *Nat. Commun.* **4**, 1463 (2013).
18. G. Chen, Skyrmion Hall effect. *Nat. Phys.* **13**, 112–113 (2017).
19. T. Moriya, Anisotropic superexchange interaction and weak ferromagnetism. *Phys. Rev.* **120**, 91–98 (1960).
20. I. Dzyaloshinsky, A thermodynamic theory of "weak" ferromagnetism of antiferromagnetics. *J. Phys. Chem. Solid* **4**, 241–255 (1958).
21. W. Koshibae, N. Nagaosa, Theory of antiskyrmions in magnets. *Nat. Commun.* **7**, 10542 (2016).
22. A. Soumyanarayanan, M. Raju, A. G. Oyarce, A. K. Tan, M.-Y. Im, A. P. Petrović, P. Ho, K. Khoo, M. Tran, C. K. Gan, F. Ernult, C. Panagopoulos, Tunable room-temperature magnetic skyrmions in Ir/Fe/Co/Pt multilayers. *Nat. Mater.* **16**, 898–904 (2017).
23. A. N. Bogdanov, U. K. Rößler, M. Wolf, K.-H. Müller, Magnetic structures and reorientation transitions in noncentrosymmetric uniaxial antiferromagnets. *Phys. Rev. B* **66**, 214410 (2002).
24. S. Huang, C. Zhou, G. Chen, H. Shen, A. K. Schmid, K. Liu, Y. Wu, Stabilization and current-induced motion of antiskyrmion in the presence of anisotropic Dzyaloshinskii-Moriya interaction. *Phys. Rev. B* **96**, 144412 (2017).
25. J. Jena, B. Göbel, T. Ma, V. Kumar, R. Saha, I. Mertig, C. Felser, S. S. P. Parkin, Elliptical Bloch skyrmion chiral twins in an antiskyrmion system. *Nat. Commun.* **11**, 1115 (2020).

26. L. Peng, R. Takagi, W. Koshibae, K. Shibata, K. Nakajima, T.-h. Arima, N. Nagaosa, S. Seki, X. Yu, Y. Tokura, Controlled transformation of skyrmions and antiskyrmions in a non-centrosymmetric magnet. *Nat. Nanotechnol.* **15**, 181–186 (2020).

27. M. Hoffmann, B. Zimmermann, G. P. Müller, D. Schürhoff, N. S. Kiselev, C. Melcher, S. Blügel, Antiskyrmions stabilized at interfaces by anisotropic Dzyaloshinskii-Moriya interactions. *Nat. Commun.* **8**, 308 (2017).

28. F. Zheng, F. N. Rybakov, A. B. Borisov, D. Song, S. Wang, Z.-A. Li, H. Du, N. S. Kiselev, J. Caron, A. Kovács, M. Tian, Y. Zhang, S. Blügel, R. E. Dunin-Borkowski, Experimental observation of chiral magnetic bobbers in B20-type FeGe. *Nat. Nanotechnol.* **13**, 451–455 (2018).

29. D. Suess, C. Vogler, F. Bruckner, P. Heistracher, F. Slanovc, C. Abert, Spin torque efficiency and analytic error rate estimates of skyrmion racetrack memory. *Sci. Rep.* **9**, 4827 (2019).

30. H. Du, R. Che, L. Kong, X. Zhao, C. Jin, C. Wang, J. Yang, W. Ning, R. Li, C. Jin, X. Chen, J. Zang, Y. Zhang, M. Tian, Edge-mediated skyrmion chain and its collective dynamics in a confined geometry. *Nat. Commun.* **6**, 8504 (2015).

31. C. Jin, Z.-A. Li, A. Kovács, J. Caron, F. Zheng, F. N. Rybakov, N. S. Kiselev, H. Du, S. Blügel, M. Tian, Y. Zhang, M. Farle, R. E. Dunin-Borkowski, Control of morphology and formation of highly geometrically confined magnetic skyrmions. *Nat. Commun.* **8**, 15569 (2017).

32. C. Psaroudaki, S. Hoffman, J. Klinovaja, D. Loss, Quantum dynamics of skyrmions in chiral magnets. *Phys. Rev. X* **7**, 041045 (2017).

33. D. Song, Z.-A. Li, J. Caron, A. Kovács, H. Tian, C. Jin, H. Du, M. Tian, J. Li, J. Zhu, Quantification of magnetic surface and edge states in an FeGe nanostripe by off-axis electron holography. *Phys. Rev. Lett.* **120**, 167204 (2018).

34. O. Meshcheriakova, S. Chadov, A. Nayak, U. Rößler, J. Kübler, G. André, A. Tsirlin, J. Kiss, S. Hausdorf, A. Kalache, Large noncollinearity and spin reorientation in the novel Mn$_2$RhSn Heusler magnet. *Phys. Rev. Lett.* **113**, 087203 (2014).

35. A. Vansteenkiste, J. Leliaert, M. Dvornik, M. Helsen, F. Garcia-Sanchez, B. Van Waeyenberge, The design and verification of MuMax3. *AIP Adv.* **4**, 107133 (2014).

36. A. Vansteenkiste, B. Van de Wiele, MuMax: A new high-performance micromagnetic simulation tool. *J. Magn. Magn. Mater.* **323**, 2585–2591 (2011).

37. L. Landau, E. Lifshitz, in *Perspectives in Theoretical Physics* (Elsevier, 1992), pp. 51–65.

38. T. L. Gilbert, A phenomenological theory of damping in ferromagnetic materials. *IEEE Trans. Magn.* **40**, 3443–3449 (2004).

Science Advances

Evolution and competition between chiral spin textures in nanostripes with D_{2d} symmetry

Jagannath Jena, Börge Göbel, Vivek Kumar, Ingrid Mertig, Claudia Felser and Stuart Parkin